Polymer Journal (2019) 51:1197–1209
https://doi.org/10.1038/s41428-019-0230-3

ORIGINAL ARTICLE

# Self-charging photo-power cell based on a novel polymer nanocomposite film with high energy density and durability

Swagata Roy[1] · Pradip Thakur[2] · Nur Amin Hoque[1] · Arpan Kool[3] · Farha Khatun[1] · Prosenjit Biswas[1] · Biswajoy Bagchi[4] · Sukhen Das[1]

Received: 10 April 2019 / Revised: 12 June 2019 / Accepted: 12 June 2019 / Published online: 1 July 2019


## Abstract

The present work emphases the fabrication of a simple, solid-state, and cost-effective multifaceted device called a "self-charging photo power bank" based on an in situ-synthesized $MgO_2$ NP-impregnated electroactive and high dielectric poly (vinylidene fluoride) thin film composite as its active material. Positioned under visible-light illumination of 110 mW/cm$^2$ and in the absence of any sort of external bias, our optimized multilayered device can self-charge to a voltage of 1170 mV in just 24 s. An excitingly high energy density of 240 mW h/m$^2$ and a remarkable charge density of 1350 C/m$^2$ along with the excellent energy-retaining power of the device for a considerable period of time illustrate its potential as an efficient power bank. The device is used for 30 consecutive days to prove its commendable long-term cycling stability. Three blue, commercial LEDs and a digital table clock are successfully powered by our device. Our fabricated device portends an innovative approach for self-generation and simultaneous storage of electrical energy, making it an efficacious nascent aspirant in the realms of energy harvesting and storage, which can undoubtedly meet the energy necessities in the imminent future.

## Introduction

Over the last few decades, electroactive polymers (EAPs) have been acknowledged by the scientific community for their outstanding contributions to the fields of actuators, acoustic transducers, membranes, nonvolatile memories, batteries, piezoelectric sensors/nanogenerators, flexible energy harvesting and storage systebiomaterials, etc [1–8]. Among all EAPs, PVDF ($CH_2$–$CF_2$) has been the most popular semicrystalline plastic because it is highly flexible and economically and ecologically nonthreatening. Although the $\alpha$ polymorph (TGTG′ dihedral conformation) of PVDF is the most thermodynamically stable nonpolar phase, the $\beta$ polymorph of PVDF, with all *trans* TTTT planar conformations, has received attention from the research community owing to its possession of a remarkably high dipolar moment per unit cell of $8 \times 10^{-30}$ Cm due to the disparity in the electronegativity of fluorine atoms and hydrogen and carbon atoms; thus this configuration exhibits the highest piezo-, pyro-, ferro-, and dielectric characteristics when matched with other polar polymorphic forms ($\gamma$ and $\delta$) of PVDF [1, 7–10].

To date, innumerable endeavors have been employed to obtain complete crystallization of a stable $\beta$-phase from the nonpolar $\alpha$ form of PVDF, but accomplishing this task is challenging. Electrospinning [11], electric and magnetic field application [12], and stretching and poling [13] of nonpolar PVDF are a few of the many techniques adopted

**Supplementary information** The online version of this article (https://doi.org/10.1038/s41428-019-0230-3) contains supplementary material, which is available to authorized users.

✉ Pradip Thakur
pradipthakurju@gmail.com

✉ Sukhen Das
sdasphysics@gmail.com

[1] Department of Physics, Jadavpur University, Kolkata 700032, India

[2] Department of Physics, Netaji Nagar College for Women, Kolkata 700092, India

[3] Department of Physics, Techno India University, Kolkata 700091, India

[4] Department of Medical Physics and Biomedical Engineering, University College London, London, UK

for $\beta$-phase augmentation. However, researchers have also initiated exploitation of various inorganic fillers, such as nanoparticles (NPs), oxide nano/micro-fillers [14–18], organic clays [19–21], CNTs [22], ceramic materials [23], ferrites [24], grapheme [25], etc., for the nucleation and significant intensification of the electroactive $\beta$-phase by impregnating these materials within the PVDF matrix. This method has provided positive results. In situ doping of PVDF layers has emerged as one of the effective trends in the promotion and enrichment of this phase, and several reports have established this method [16, 26]. However, a thorough literature survey could not find a single report on in situ doping with $MgO_2$ NPs in PVDF. A prototype approach for synthesizing $MgO_2$/PVDF composite thin films by a fast and facile in situ doping process has been studied in our present work. To produce a series of $MgO_2$/PVDF films, varying concentrations and molar ratios are considered. The exploration of the role of $MgO_2$ NPs as the active phase nucleator of PVDF and the creation of large quantities of dipoles at the onset of $MgO_2$ nanofiller impregnation, leading to interfacial polarization and contributing to the enhancement of the dielectric constant and energy storage aptitude, are crucial perspectives of our study. Our investigation is unique owing to both these insights, which further elucidate fresh opportunities in piezoelectric nanogenerators and the energy harvesting and storage industry.

The current situation indicates a severe predicament due to plentiful interlinking relationships in the provinces of energy and power requirements and the steady exhaustion of limited natural resources such as coal, petroleum, etc. With the ever-increasing population, demands in the energy sectors will magnify and become reasonably challenging to realize. Thereafter, the world's energy groundwork is at stake and can be replenished only by exploiting inexhaustible and environmentally benign solar energy [8, 27–31].

To harness solar energy, its simultaneous photoelectric conversion and implementation in various energy storage devices has attracted attention from modern day researchers. The fabrication of solar devices with a photovoltage generation unit using a dye absorbing source has been reported in several works [32–34]. Some studies have been reported in the domains of photochargeable energy storage devices, which consist of separate units of both light energy harvesting (photovoltaic/solar cell) and storage system (lithium-ion batteries and supercapacitors) units together [35–39]. The total increase in the resistances and inappropriate regulation of light input severely decrease the energy output values in such integrated devices [40, 41]. Nevertheless, this energy dearth can be surpassed by the appropriate integration of the energy production and storage units into a single unit, which may minimize this energy loss problem. Few efforts have been incorporated to fabricate such devices. In one work, a photosupercapacitor was engineered by integrating an organic photovoltaic device with a CNT-based supercapacitor into a single unit, which overcomes the internal resistance and power loss to a great extent [40, 42].

The newly synthesized electroactive and high dielectric $MgO_2$/PVDF nanocomposite thin films and their utilization in solar energy capture and storage for the operation of various electronic gadgets are the sole focus of our present investigation. Our study introduces $MgO_2$ NPs for the first time as a successful filler for phase modification of PVDF. Apart from the polar phase transformation of PVDF and its enhancement to a remarkable extent, the dielectric constant of PVDF was also enhanced, increasing its storage properties. The device fabricated using $MgO_2$/PVDF nanocomposite thin films as an active material assisted by a photon-absorbing dye composite film can prove to be quite promising due to its low weight and simple nature. The current study proposes a novel and combined methodology for light energy harvesting and storage.

## Experimental

### Materials

Precursor materials used in our work include chemicals viz. poly(vinylidene fluoride) (PVDF) pellets (Aldrich, Germany, Mw = 275,000 GPC; Mn = 110,000), dimethyl sulfoxide (DMSO) (Merck India), magnesium chloride hexahydrate ($MgCl_2{\cdot}6H_2O$) (Merck, India), sodium borohydride ($NaBH_4$) (Merck, India), polyvinyl pyrrolidone (PVP) (Lobachemie, India), eosin yellow ($C_{20}H_6Br_4Na_2O_5$), (Lobachemie, India), $TiO_2$ and CdS NPs (synthesized NPs; see Supporting Information), and conc. sulfuric acid ($H_2SO_4$; 98% pure, Merck, India). Commercially procured glass-coated FTO substrates and aluminum foil from Sigma-Aldrich, USA are the electrodes used in this study. Apart from the preparation of a 10% solution of sulfuric acid in DI water, all these supplies are employed as purchased without going through any further supplemental alteration.

### In situ synthesis of $MgO_2$ NP-modified PVDF (MP) composite films

A simple preparative solution casting route is adopted to synthesize pure and $MgO_2$ NP-loaded PVDF films. PVDF solution (5% PVDF in 5 mL DMSO at 60 °C) is taken in a culture tube, and magnesium chloride hexahydrate ($MgCl_2{\cdot}6H_2O$) (c.f. Supporting Information Table 1) is added to it with constant magnetic stirring. Then, 1 M sodium borohydride solution prepared in DMSO is slowly

added dropwise to the previous solution, and the stirring continues for another 12 h at the same temperature. The reducing agent $NaBH_4$ is responsible for the transformation of the metal to its respective oxide in air at ambient temperature. $MgO_2$ NP-modified PVDF thin films are procured by pouring the solution on clean glass plates placed in a dirt-free hot-air oven and drying them by complete evaporation of DMSO at a temperature of 80 °C for 24 h. Sealable enclosures are used to protect the synthesized films from moisture exposure prior to advance characterization and device fabrication.

## SPPB fabrication

FTO-coated glass plates (pretreated with acetone/distilled water (DI) and air dried) and aluminum foils are used as positive and counter electrodes, respectively, for our device fabrication. First and foremost, a dye solution is obtained by mixing 10 mg/mL each of eosin Y, $TiO_2$ NPs, and CdS NPs along with 10 mass % PVP in DI water with stirring at ambient temperature. Furthermore, dilute sulfuric acid (10% acid in water by volume) is gradually added to the solution and stirred overnight to attain good uniformity. A viscous orange thin layer of dye film is attained when 20 µL of the aforementioned suspension is drop-casted on the conducting side of FTO glass, which constitutes the solar part of our SPPB device. Our optimized in situ-synthesized $MgO_2$/PVDF thin film (MP 0.09) with a thickness of ~20 µm and dimensions of $0.3 \times 0.3$ cm is also cast on aluminum foil. Then, the film is sandwiched neatly atop the viscous dye film and dried at 60 °C for quick evaporation of excess water and to secure contacts between the solar and storage parts. Parallel preparations are carried out for devising our control device SPPB1 by simply substituting the storage part with an unadulterated PVDF film to compare the photovoltage results. Cu wires are attached at either end of both electrodes for subsequent photovoltage measurements.

## Sample characterizations and measurements

Proper growth of $MgO_2$ NPs, their leverage in the electroactive $\beta$-phase crystallization in all the in situ-synthesized MP composite films and their thermal behaviors are characterized by an X-ray diffractometer (Model-D8, Bruker AXS Inc., Madison, WI) using nickel-filtered Cu-$K_\alpha$ radiation from 10° to 60° 2θ values, a Fourier transform infrared spectrometer (FTIR-8400S, Shimadzu) in the wavenumber range from 400 $cm^{-1}$ to 1000 $cm^{-1}$ with a 4 $cm^{-1}$ resolution and 50 scans per sample and differential scanning calorimetry (DSC-60, Shimadzu (Asia Pacific) Pte Ltd, Singapore) at an increasing rate of 10 °C/min under a $N_2$ gas atmosphere.

Beer–Lambert law is used for the estimation of the amount of $\beta$-phase transformation from FTIR spectra and is given by

$$F(\beta) = \frac{A_\beta}{\left(\frac{K_\beta}{K_\alpha}\right)A_\alpha + A_\beta}, \quad (1)$$

where $A_\beta$ = the absorbance at 840 $cm^{-1}$, $A_\alpha$ = the absorbance at 764 $cm^{-1}$, and $K_\beta = 7.7 \times 10^4 cm^2 mol^{-1}$ and $K_\alpha = 6.1 \times 10^4\ cm^2\ mol^{-1}$ are the absorption coefficients at 840 $cm^{-1}$ and 764 $cm^{-1}$, respectively [4, 8, 24].

Sample images are captured, and the corresponding morphologies are analyzed by FESEM (INSPECT, F50, Netherlands) operating under an emission current of 170 µA and an operating voltage of 20 kV.

A digital LCR meter (Agilent, E4980A) is employed to explore the dielectric properties viz. dielectric constant ($\varepsilon$), tangent loss (tan $\delta$), and AC conductivity ($\sigma_{ac}$) of the pure PVDF and $MgO_2$ NP-embedded PVDF thin films in the frequency range from 20 Hz to 2 MHz under a 1-V AC voltage signal.

The equations involved in the calculation of the dielectric constants and AC conductivity of the synthesized MP composite films are as follows:

$$\varepsilon = C{\cdot}d/\varepsilon_0 A \quad (2)$$

$$\sigma_{ac} = 2\pi f \varepsilon_0 \varepsilon \tan\delta, \quad (3)$$

where $C$ is the capacitance, $A$ is the area, $d$ is the thickness, tan $\delta$ is the tangent loss of the film samples, $f$ stands for the applied frequency in Hz, and $\varepsilon_0$ denotes the permittivity of free space with the value $8.854 \times 10^{-12}\ F\ m^{-1}$ [8, 20, 21, 26].

A 40 W tungsten filament lamp and a multimeter (Agilent U1252A) are used to study the photovoltaic performance of the optimized $MgO_2$/PVDF nanocomposite film.

Equations involved in the computation of the energy density ($E_D$), charge density ($Q_D$), areal capacitance ($C_A$), and power density ($P_D$) of our fabricated device are given by

$$J_D = V_m/(R \times A) \quad (4)$$

$$E_D = \left(C_A \times V_m^2\right)/2 \quad (5)$$

$$Q_D = \int J_D.dt \quad (6)$$

$$C_D = \left(\int J_D.dt\right)/dV \quad (7)$$

$$P_D = V_m \times J_D, \quad (8)$$

where $V_m$ is the maximum voltage attained by the device, $J_D$ is the discharge current density, $A$ is the area of the film considered, $R$ is the resistance, and $dV$ is the difference in the discharge potential. All the characterizations are accomplished at room temperature and atmospheric pressure [8, 41].

## Results and discussion

### Analysis on electroactive β-phase identification

With the aim of having a detailed and comparative study on the formation and nature of the development of the electroactive $\beta$-phase in PVDF after its matrix is modified by increasing concentrations of in situ-synthesized $MgO_2$ NPs, X-ray diffraction, FTIR, DSC, and FESEM studies were performed.

The diffraction patterns illustrated in Fig. 1a marked by the prominent blue line patches at $2\theta = 17.5°$ (100), 18.2° (020), 19.9° (021), and 26.5° ((201), (310)) finely elucidate the existence of crystalline $\alpha$-phase reflections in pure PVDF [1, 8, 16, 20]. On the other hand, due to the influence of the in situ dopant in the polymer matrix, the characteristic peaks at $2\theta = 31.9°$ (111), 41.5° (210), and 45.7° (211) in the spectra indicate the proper formation of $MgO_2$ NPs embedded inside the polymer layers (JCPDS card no: 761363). The oxidation state of Mg in the magnesium peroxide ($MgO_2$) NP/PVDF composite film is +2. The peroxide groups are designated by $O_2^{2-}$, which is bonded with $Mg^{2+}$ to form the $MgO_2$ NPs. Eventually, a new phase recognized as the electroactive $\beta$-phase appears with peaks at $2\theta = 20.7°$ ((110), (200)) and 36.5° ((020), (100)) in the $MgO_2$ NP-modified PVDF (MP) spectra with the simultaneous disappearance of all the larger α-spherulites [1, 7, 8]. According to JCPDS-761363, $MgO_2$ also has a peak at 37.1°, which is in close proximity to the position of the $\beta$-phase peak. Therefore, the isolated presence of this peak of $MgO_2$ is not significant. Hereafter, a definite $\beta$-phase transformation from nonpolar $\alpha$ crystals and its augmentation with the doping concentration relative to pure PVDF are confirmed. The highest $\beta$-phase content was found for the sample ~3.37 wt% (MP 0.03). Following a slight decrease, these values saturate at the higher doping concentrations. Good homogenous dispersal of the $MgO_2$ catalytic agents due to its fine intercalation within the inner sheets of the polymer resulting in the long-range TTTT conformation can be accredited for the molecular reorientation of the PVDF structure and increase in the $\beta$-phase. Agglomerated deposits of the dopant within the polymer matrix, however, lead to a slight decrease in the intensity of $\beta$-phase with a further increase in the doping concentration. The intensity ratios ($I_{20.7}/I_{18.2}$) portrayed in Fig. 1b signify the quantity of $\beta$ and $\alpha$ phase present in the pure and composite films. A sharp rise in this ratio to a maximum value of 15.08 is observed for the sample MP 0.03 with 3.37wt% loading, from only 0.89 in the case of pristine PVDF, validating the enhancement of $\beta$-phase nucleation.

The presence of all plausible absorbance peaks of the nonpolar $\alpha$-phases in the pure PVDF film as well as those of

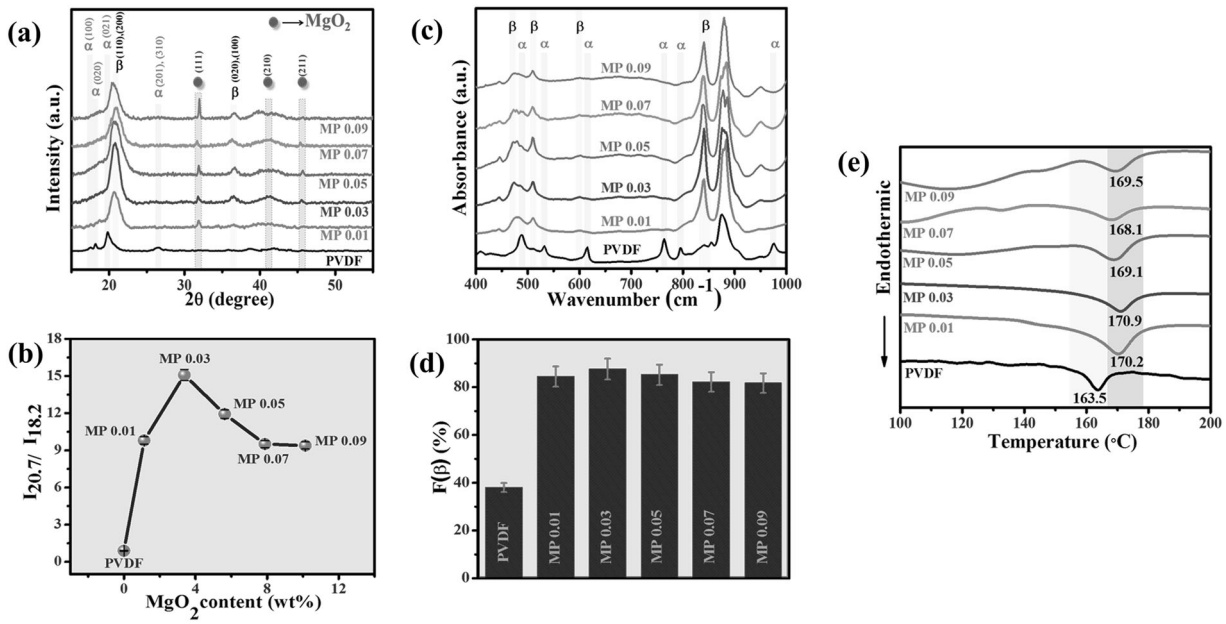


**Fig. 1** **a** X-ray diffraction patterns of neat PVDF and MP thin films. **b** Ratio of $I_{20.7}$ and $I_{18.2}$ of the neat PVDF and MP thin films. **c** FTIR spectra of neat PVDF and MP thin films. **d** Evaluation of the *F (β)* (%) of neat PVDF and MP thin films. **e** DSC thermographs of neat PVDF and MP thin films

the prominent polar $\beta$-phases in $MgO_2$/PVDF films in the FTIR spectra (cf. Fig. 1c) shows the high volumes in establishing the enrichment of the electroactive $\beta$-phase nucleation in the MP composite films. The absorbance peaks characteristic of nonpolar $\alpha$-crystallites in the spectra of neat PVDF are visible at 488 $cm^{-1}$ ($CF_2$ waging), 532 $cm^{-1}$ ($CF_2$ bending), 614 $cm^{-1}$ and 764 $cm^{-1}$ ($CF_2$ bending and skeletal bending), and 796 $cm^{-1}$ and 975 $cm^{-1}$ ($CH_2$ rocking), entirely disappear, whereas the intensity of the small absorbance peak of the $\beta$-crystal at 840 $cm^{-1}$ ($CH_2$ rocking, $CF_2$ stretching, and skeletal C–C stretching) steadily increases in intensity with the increase in the weight percentage of additives in the PVDF matrix. Furthermore, the FTIR spectra also illustrate a notable upsurge in the absorption bands of the $\beta$ polymorphs at 479 $cm^{-1}$ ($CF_2$ deformation), 510 $cm^{-1}$ ($CF_2$ stretching), and 600 $cm^{-1}$ ($CF_2$ wagging) [1, 4, 8, 16] in the $MgO_2$ NP-modified PVDF films, suggesting effective $\beta$-phase crystallization. It is quite interesting to note that only a small amount, i.e., ~1.12 wt% of $MgO_2$ NPs (MP 0.01), can initiate $\beta$-phase nucleation in the MP composite films, with the highest absorption at 840 $cm^{-1}$ being for ~3.37 wt% (MP 0.03). The homogeneous distribution of the $MgO_2$ NPs entrenched within the polymer layers allow them to act as fine catalytic agents, shaping the improvement in the electroactive $\beta$-crystallites in the $MgO_2$/PVDF films. In contrast, internment in the movements of the PVDF chains impedes long TTTT chain formation, leading to the attenuation of the $\beta$-phase with further doping of the NPs in the PVDF matrix. The quantification of the electroactive $\beta$-phase content $F(\beta)$ in the pristine and doped composite thin films is computed by Beer–Lambert law, which is previously mentioned as equation (1). The escalation of $F(\beta)$ values from only 38% in the case of PVDF to a maximum value of ~87% at 3.37 wt% loading in the MP 0.03 sample is documented by the histograms in Fig. 1d. All of these FTIR results are in good agreement with the XRD data, indicating that $\beta$-phase nucleation is greatly accelerated by the incorporated nanofillers.

In conjunction with the phase study, the thermal behavior of the diverse crystalline phases of the pure and MP composite samples can also be well explained by the DSC thermograms. The prominent endothermic peak at 163.5 °C in Fig. 1e marks the obvious occurrence of nonpolar $\alpha$-phase crystals in pristine PVDF [8, 16, 41]. Nonetheless, the melting peak ($T_m$) shifts to the higher temperature side ($T_m$) by 5–7 °C once the fillers are embedded in the polymer layers. Strong electrostatic interactions between the in situ-synthesized $MgO_2$ NP surface and the $CH_2$/$CF_2$ groups of PVDF chains and the simultaneous formation of long TTTT chains of $\beta$ polymorphs in the composites due to the incorporation of NPs play an important role in the nucleation process, resulting in the transformation of the polar $\beta$-form from its nonpolar state, ensuring a notable upshift in the endothermic peaks [8, 26]. Closer observation shows some heat absorption near 100–120 °C in the DSC curves of MP 0.07 and MP 0.09, which might be due to evaporation of absorbed moisture in the surface of the samples from the atmosphere during the measurements. DSC analysis is an effective complementary technique to XRD and FTIR in establishing the nucleation and augmentation of the electroactive $\beta$ crystals in the in situ $MgO_2$ NP-modified PVDF thin films.

Strong supporting evidence for the successful growth of $\beta$ spherulites with the impregnation of $MgO_2$ dopants into a polymer matrix can be obtained through FESEM morphological images, which once again corroborate with the previous XRD, FTIR, and DSC analyses. Large nonpolar $\alpha$ spherulites ranging in diameters from 30 to 60μm constitute the matrix of neat PVDF (see Supporting Information Fig. S3). However, the picture alters significantly with the incorporation of $MgO_2$ nanofillers into the PVDF matrix. Figure 2a–e demonstrates the uniform distribution

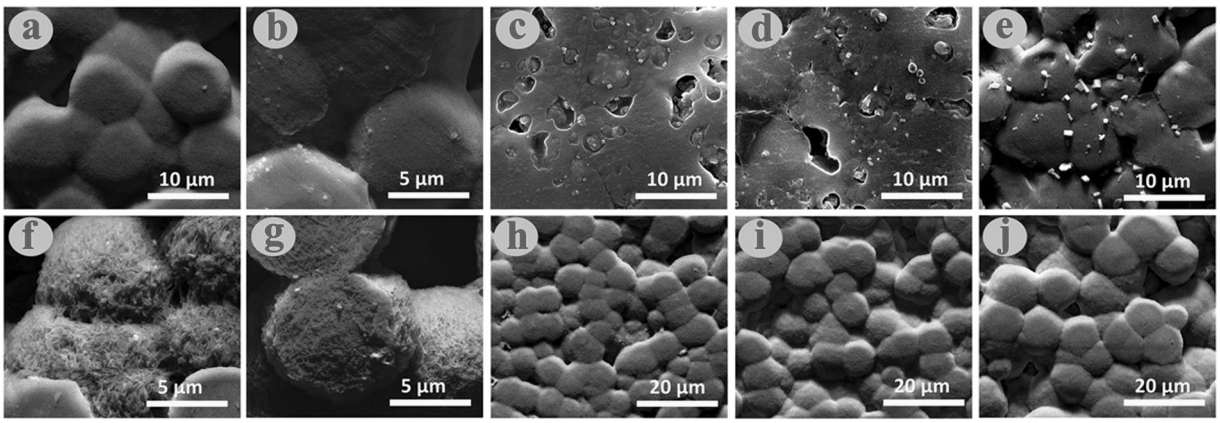


**Fig. 2** FESEM micrographs (**a**, **b**, **c**, **d**, **e**) showing different weight % of MP thin films with evenly distributed in situ-synthesized $MgO_2$ NPs in a PVDF matrix and (**f**, **g**, **h**, **i**, **j**) the formation of $\beta$ spherulites in different weight % of MP thin films

of the in situ-synthesized $MgO_2$ NPs with dimensions of ~150–300 nm over the polymer matrix with intense clarity. The FESEM image of the fractured surface of the $MgO_2$/PVDF composite film with the highest doping concentration, i.e., MP 0.09, is provided in Fig. 3a, which clearly illustrates the homogeneous distribution of $MgO_2$ NPs within the PVDF matrix. The graphical representation of the particle size distribution of the $MgO_2$/PVDF nanocomposite film is also provided in Fig. 3b with a Gaussian fitting to ascertain the range of the particle size distribution in the film sample. The consistency in the filler dispersal definitely helps in the enrichment of the polar $\beta$-phase crystallization. The presence of well demarcated smaller spherulites ~3–5 μm in size (c.f. Fig. 2f–j) [7, 8, 14] is also strong evidence of this phase transformation throughout the matrix.

## Dielectric analysis

Notably, changes in the dielectric properties, i.e., the dielectric constant ($\varepsilon$), tangent loss ($\delta$), and AC conductivity

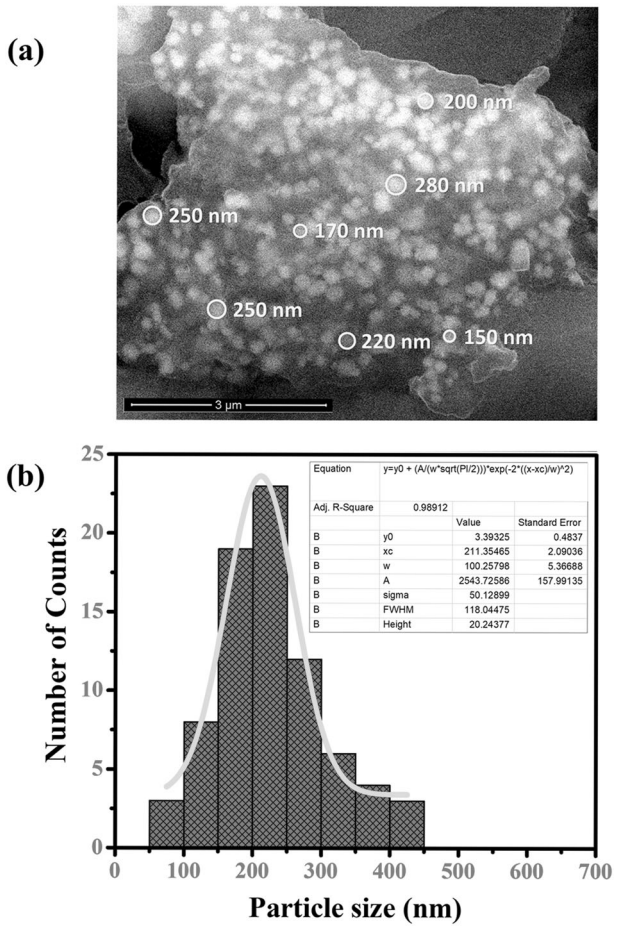


**Fig. 3** **a** FESEM image of the fractured surface of $MgO_2$/PVDF nanocomposite thin film (MP 0.09); **b** particle size distribution of the nanocomposite film with Gaussian fitting

($\sigma$), of pure PVDF after permeation by in situ-synthesized $MgO_2$ NPs are obvious from the graphical illustrations depicted in Fig. 4, which are computed using two well-known equations (2) and (3). Graphs plotted in Fig. 4a, b with respect to the weight % content of additives are shown for a number of frequencies, i.e., 20 Hz, 100 Hz, 10 kHz, and 1 MHz. The value of the dielectric constant progressively increases (cf. Fig. 4a) with the rise in the doped concentration of $MgO_2$ NPs in PVDF until the doping content reaches 7.88wt% (MP 0.07) and its percolation threshold, resulting in a sudden maximum value of $2.7 \times 10^6$ for the maximum doping concentration of 10.13wt% (MP 0.09) for 20 Hz. This achieved value of the dielectric constant is startlingly high, i.e., $\sim 3 \times 10^5$ times greater than the dielectric value of pure PVDF, i.e., 9 [1, 7, 16], whereas the tangent loss recorded corresponding to the highest dielectric constant at 20 Hz is only 15 times (approximately) greater than that of PVDF at the same frequency. Electrons tunnel out from one $MgO_2$ NP surface to its adjacent surface, initiating a conducting chain system may contribute to dielectric escalation [41, 43]. Other higher frequencies also exhibit feeble yet identical styles of dielectric intensification with the doping concentration. Agglomeration of NPs decreases the interfacial surface area with further dopant increases, and further increases in the dielectric constant are restricted due to the generation of surface pores and degradation of the material's surface integrity [8].

Maxwell–Wagners–Sillars (MWS) polarization is predominant in the lower frequency range and strongly edifies the enhancement of the dielectric constant. Because of the incongruence in the conductivities of the NPs and the polymer surfaces, at the onset of an external alternating electric field, all the charge particles/dipoles quickly move with the intent of substantial accumulation and simultaneous deposition, resulting in a large localized interfacial polarization at the interface created between the aforementioned heterogeneous media. The reduction in the intermolecular distance, the increase in the interfacial area for each unit volume associated with both the NPs and polymer surface, the enrichment of the $\beta$-phase (*all trans* TTTT long chains) with the increase in the dopant density within the PVDF and the simultaneous appearance of abundant small range dipoles all confirm the excellent embedment and fine homogeneity of the NPs in the layered polymer matrix as well as substantial charge deposition at the interface. This charge deposition leads to a large increase in the dielectric value of the doped samples relative to that of PVDF [1, 8, 41, 44, 45]. Graphical illustrations in Fig. 4c underscore a dramatic decrease in the dielectric constant with increasing frequency. This fact can be explained by dipolar polarization, which controls the higher frequency range. At this juncture, otherwise randomly oriented dipoles/charge carriers are positioned in the direction of the field but its

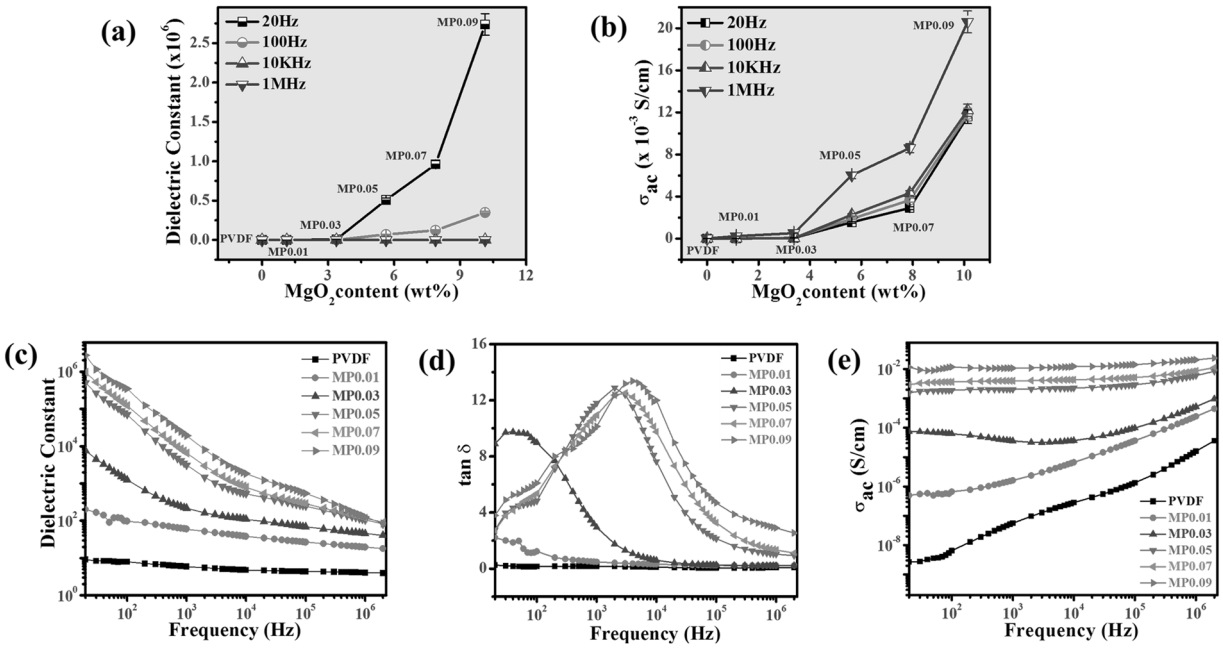


**Fig. 4** $MgO_2$ NP content (weight %) dependency of the **a** dielectric constant and **b** AC conductivity at different frequencies of neat PVDF and MP thin films. Frequency dependency of the **c** dielectric constant, **d** tangent loss, and **e** AC conductivities of neat PVDF and MP thin films

polarizing ability decreases as the dipoles cannot continue to follow its pace and have an effective lag with reference to the high frequency of the electric field. Then, a sharp reduction in the number of dipoles along with the dipole movement internment follow, resulting in a decrease in the dielectric value of the material in the higher range of frequency [8, 16, 45].

Dampened oscillations of electric dipoles originating from heat loss and intermolecular hopping of electrons are responsible for the tangent losses in samples. The Debye-like relaxation peaks obtained (cf. Fig. 4d) are considerably trivial when compared to the large dielectric values. However, our synthesized samples are good dielectric materials with low loss. A prominent right shift in this tangent loss is noted in the higher frequency range with the increase in the concentration. Strong dipolar relaxation resulting from the strong ion–dipole interaction of $MgO_2$ NPs with the $CH_2$/$CF_2$ polymer chains is likely the cause of this shift [8, 46].

The AC conductivity, as shown in Fig. 4b, has an overall increase with the frequency and loading weight content of $MgO_2$ NPs, exhibiting the highest conductivity for 10.134 wt% loading. Therefore, substantial charge accumulation by MWS polarization and dipolar relaxation contributes to the improvement in the AC conductivity with the loading concentration [8, 44, 45]. Careful observation reveals that although the AC conductivities of the samples with lower doping percentages (MP 0.01 and MP 0.03) inclusive of PVDF show a prominent increase with frequency; for samples with higher doping concentrations (MP 0.05, MP 0.07, and MP 0.09), the conductivity is almost independent of frequency, establishing the good frequency stability of these materials (cf. 4 (e)). The lower and higher frequency zones are regulated by the DC conductivity and AC conductivity, respectively. The disappearance of the lower frequency plateau in Fig. 4e due to rapid and linear growth in the conductivity confirms the pure AC characteristic of the conductivity for all synthesized composite films [8, 45].

## Performance of SPPB and its detailed mechanism

Thus far, our study has established that sample MP 0.09 possesses the highest dielectric value on the order of $10^6$ at 20 Hz, indicating a high storage efficacy along with a notable $\beta$-phase transformation of approximately an $F(\beta)$ value of 82%. In the search for a material that is a combination of both attributes, MP 0.09 promises to fulfill both and is a good candidate for our device fabrication. The device named "self-charging photovoltaic power bank" is abbreviated as SPPB2 for convenience. The control device fabrication is carried out with pure PVDF for a comparative study and named SPPB1.

A diagram illustration of the step-by-step mechanism of the device formation along with its digital photographs is presented in Fig. 5. The light-receiving areas for both films (PVDF and MP 0.09) with thicknesses of ~25 μm each are $9 \times 10^{-2}$ $cm^2$ and are exploited as the active materials for devices SPPB1 and SPPB2, respectively. Two separate composite films comprising EY/CdS/$TiO_2$/PVP/$H_2SO_4$ and

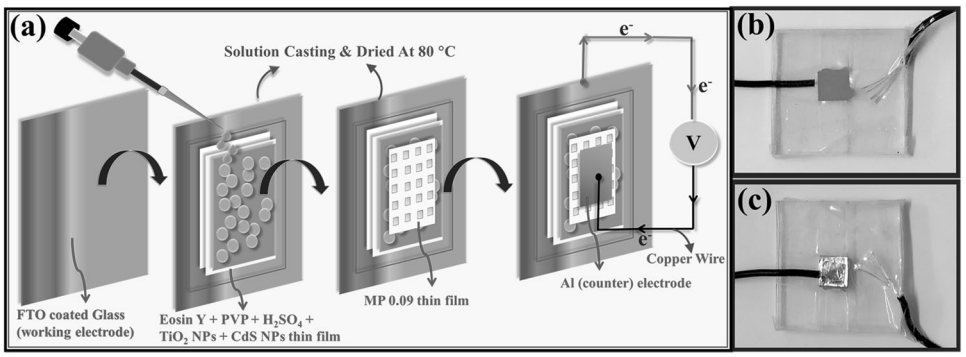


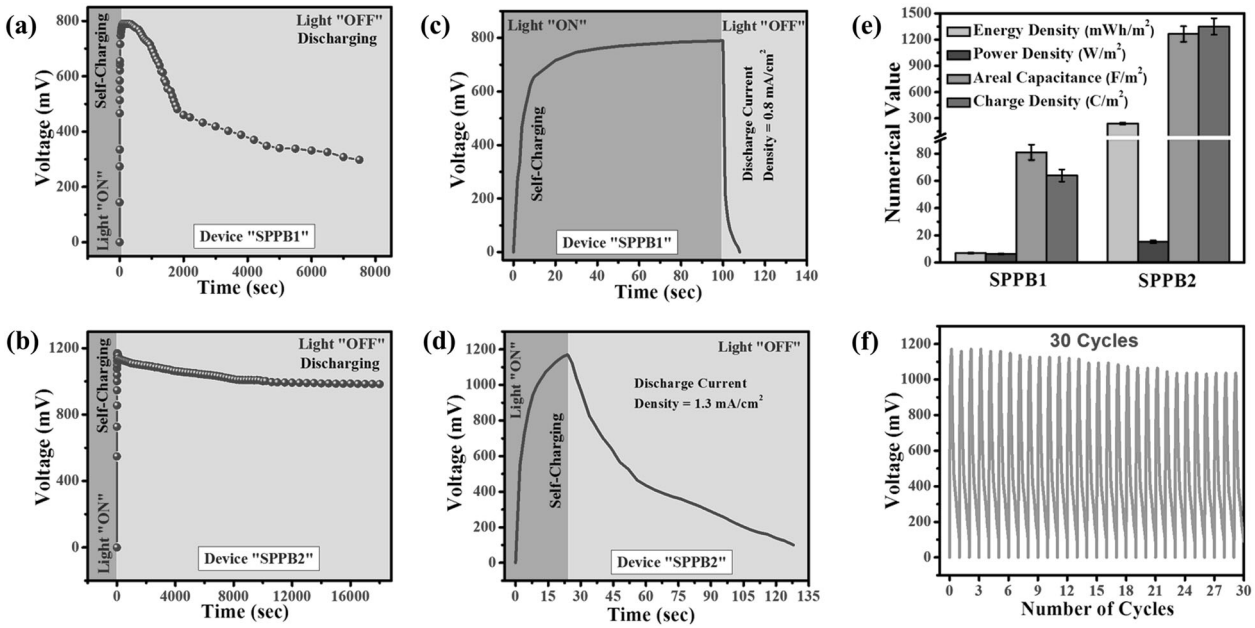


**Fig. 5** **a** Pictorial schematic of the SPPB device fabrication. **b** Digital images of both sides of the SPPB device

**Fig. 6** Self-charging and spontaneous discharging (*V–t*) graphs of the device **a** SPPB1 and **b** SPPB2 in light and dark conditions; self-charging and discharging (*V–t*) graphs of the device with a constant current density **c** SPPB1 and **d** SPPB2 as a function of time in light and dark conditions; **e** histograms demonstrating the energy density, power density, areal capacitance, and charge density of SPPB1 and SPPB2; **f** self-charging and discharging recurrence cycle of device SPPB2

in situ-impregnated $MgO_2$/PVDF (MP 0.09) correspondingly constitute the "solar part" and the "storage part", making them the two unique components of our device. Coupling these two units, which are sandwiched between the two electrodes, completes our device construction.

Figure 6a–d displays the self-charge–discharge (*V–t*) plots, which show the proficiency of the acquired voltage of our fabricated device SPPB2 over that of SPPB1.

The device is irradiated under a 40 W tungsten filament lamp (110 mW/cm$^2$), and within just 24 s, the device is observed to acquire a maximum voltage of 1.17 V. The next outstanding feature witnessed is the memory of device SPPB2, as it holds the voltage achieved for a remarkably long period of time (cf. Fig. 6b). The recorded self-discharge characteristics unveil that the voltage barely drops and gradually saturates even after illumination ceases and darkness encompasses the device. This behavior indicates the good stability of SPPB2. It should be mentioned here that the device is working in the presence of only visible light (ultraviolet as well as infrared eliminator filters are attached to the source), which is the sole driving force for output voltage generation. Photon absorber EY molecules and CdS NPs of the photoelectrode EY/CdS/$TiO_2$/PVP/$H_2SO_4$ film are used for photocharging purposes, and any means of external biasing is absent. Hence, SPPB2 can establish itself as a successful SPPB. SPPB1 charges up to 790 mV in 100 s and is found to have a weak memory in restoring the acquired voltage for a sufficiently longer period of time than SPPB2 (cf. Fig. 6a, b). The high dielectric value of the $MgO_2$ NPs in the PVDF (MP 0.09) film (cf. Fig. 4a, c) compared to that of only the PVDF film empowers the high storage capability of SPPB2.

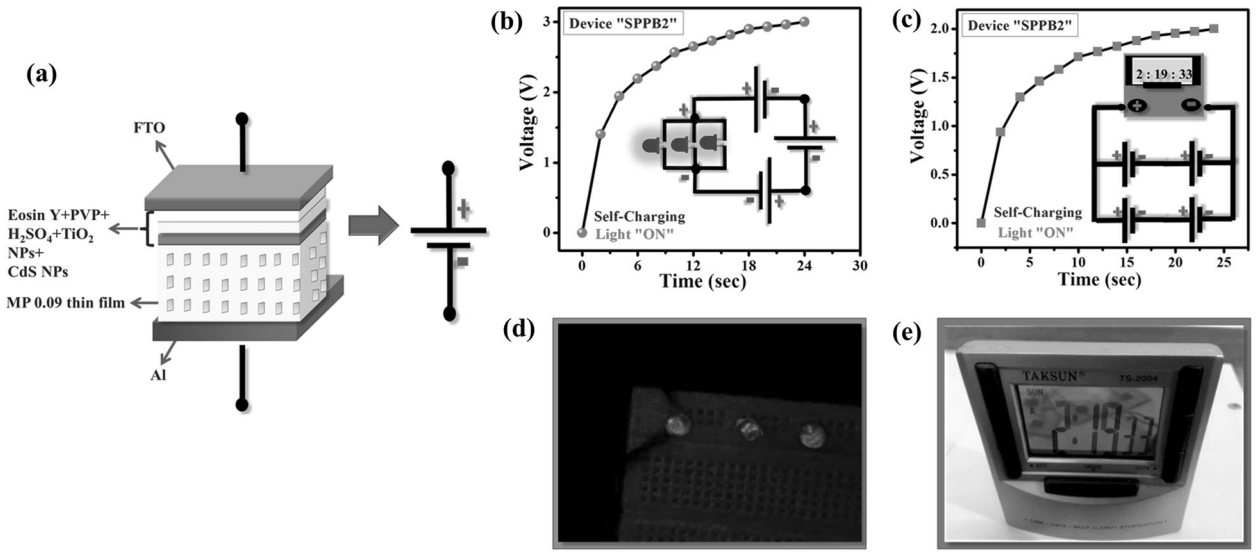


**Fig. 7** **a** Schematic of the device SPPB2 used as a cell/battery. **b** Self-charging (*V*–*t*) graph of three serially connected SPPB2s under illumination along with its schematic circuit diagram for lighting three commercial, blue LEDs using three self-charged devices. **c** Self-charging (*V*–*t*) graph and the schematic circuit diagram for the functioning of the display screen of a digital table clock using four self-charged SPPB2s under illumination in series–parallel connection. **d**, **e** Digital photographs of three lighted LEDs and working digital table clock

Discharged with a constant current density of ~1.3 mA/cm$^2$, the acquired voltage of SPPB2 decreases to a minimum of 100 mV in ~104 s, whereas SPPB1 reaches its initial voltage within 8 s with only a discharge current of ~0.8 mA/cm$^2$ (cf. Fig. 6c, d). This discharging is carried out in the absence of light.

Computed using equation 15, the well-defined histograms (cf. Fig. 6e) indicate an impressive value of energy density ($E_D$) of 240 mW h/m$^2$ for the SPPB2 device. This value claims to be almost 34 times that of SPPB1. The charge density ($Q_D$), areal capacitance ($C_A$), and power density ($P_D$) of our fabricated device SPPB2 are also simultaneously assessed using equations (16–18), and the values obtained are 1350 C/m$^2$, 1264 F/m$^2$, and 15 W/m$^2$, respectively. These values are noticeably higher than those of SPPB1.

The obtained data for all measured entities of SPPB2, i.e., the energy density, power density, charge density, and areal capacitance, are superior to the previously reported data from elaborate literature surveys [8, 37, 47, 48] (also see supporting information Table 2) in related energy storage fields, making our device distinguishable from other devices.

Figure 7a portrays a symbolic representation of our device SPPB2 for diagrammatic simplification. At times, a single device fails to facilitate the voltage and current requirements of electronic devices, and then, a series/parallel combination of devices is needed. The series assembly of three SPPB2 devices is self-powered under the same illumination, and as anticipated, the maximum voltage attained by them is ~3 V. Figure 7b, d illustrate the series combination of three SPPB2 power banks and how they power three commercial blue LEDs connected in parallel to both of the ends of the banks. The LEDs light up instantly and are seen to sustain their glow for a long time (see supporting Video V1). Similarly, to satisfy the current needs, four SPPB2 are joined in a series–parallel connection, self-charged to a maximum voltage of ~2 V and are capable of delivering a higher current. This combination can store adequate charge to operate a digital clock for a sufficient amount of time (see supporting Video V2). The pictorial illustration as well as the captured images of the digital clock in operation is displayed in Fig. 7c, e.

A colorful schematic of the operating and charging mechanism with a strong emphasis on the electron–hole transport phenomenon occurring in the fabricated device is presented in Fig. 8a. The fabricated device SPPB2 is discharged for a sufficient duration under a dark environment before being placed under an illumination of 110 mW/cm$^2$. As soon as visible-light energy is incident on the device, the EY molecules and CdS NPs present in the photoelectrode, made up of the EY/CdS/$TiO_2$/PVP/$H_2SO_4$ dye composite, start absorbing the photons of particular wavelengths (~494 and 532 nm) shown by the UV–vis spectra of the dye component in Fig. 8b. The photoexcited electrons of EY henceforth jump from its HOMO (−5.0 eV) to its LUMO (−2.5 eV) energy state, while the electrons of the CdS NPs are excited from its corresponding HOMO (−6.2 eV) to its LUMO (−3.9 eV) state. Hereafter, both EY and CdS are excited to EY* and CdS*, donate their electrons and

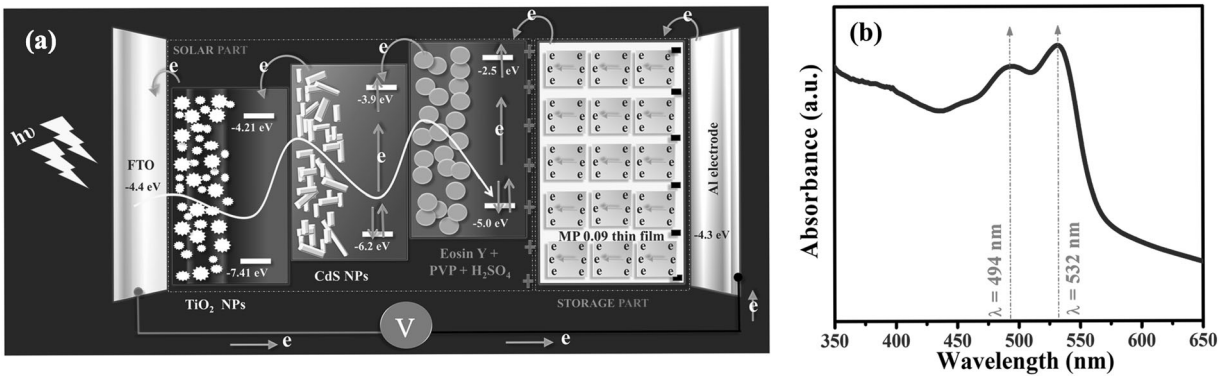


**Fig. 8** **a** Schematic representation of the self-charging and simultaneous storage mechanism in our fabricated device SPPB2. **b** UV–visible spectrum of EY/$TiO_2$/CdS/PVP/$H_2SO_4$ thin film

eventually transform into their oxidized states $[EY]_{ox}$ and $[CdS]_{ox}$ during the charging process, as shown in the following reactions (i) and (ii).

$$EY + h\upsilon \rightarrow EY* \rightarrow [EY]_{ox} + e^- \quad \text{(i)}$$

$$CdS + h\upsilon \rightarrow CdS* \rightarrow [CdS]_{ox} + e^- \quad \text{(ii)}$$

These photogenerated electrons are further inoculated into the conduction bands of CdS NPs with an energy state of −3.9 eV and into adjacent $TiO_2$ NP (−4.21 eV) bands through which they navigate to reach the photoelectrode FTO with an energy state of −4.4 eV.

Electron–hole recombination is circumscribed with the introduction of CdS NPs and $TiO_2$ NPs into the dye matrix. The easy flow of photogenerated electrons to the working FTO electrode is enhanced, which in turn improves the device performance [49, 50]. During photocharging, injected electrons at the FTO travel along the outer circuit through the Cu wire and reach the counter (Al) electrode. Employing the high dielectric and electroactive MP 0.09 composite film (dielectric constant ~$2.7 \times 10^6$) between the dye film and Al electrode restricts easy recombination of the electrons expelled from the dye content, leading to a charge difference. The $MgO_2$ NPs infused in PVDF (storage part) enrich its dielectric value to a great extent and create small charge storage centers in the polymer matrix, resulting in substantial electrical energy storage [41]. A surplus of negative photoelectrons is instantaneously amassed at the juncture of the Al electrode and MP 0.09 film and in between the seams of the $MgO_2$ NPs and PVDF, while the photogenerated holes in the EY and CdS gather at the periphery of the FTO, concluding the photocharging process of SPPB2. The maximum open circuit voltage generation of 1.17 V in the completely charged condition of our device can be ascribed to the large charge separation of electrons and holes at both ends of the film. EY and CdS NPs (solar part), which are in their oxidized states, i.e., $[EY]_{ox}$ and $[CdS]_{ox}$, due to their deficit of electrons, now accept electrons from the immediate solid electrolyte PVP/$H_2SO_4$. PVP and $H_2SO_4$ assist in transportation of the charges for recombination and act as ionic mediators when the discharging process is taken into account. Their redox states are also clearly mentioned in the equations below [40].

Then, EY/CdS are replenished and reduced, return to their original states and are capable of once more absorbing photons. They become photosensitized and release additional photoelectrons to repeat the entire process without halting [8, 37, 41, 47, 48]. The following equations [(iii)–(x)] can provide an understanding of the reactions occurring in the process.

$$PVP + e^- \leftrightarrow PVP^- \quad \text{(iii)}$$

$$H_2SO_4 \rightarrow 2H^+ + SO_4^{2-} \quad \text{(iv)}$$

$$[EY]_{ox} + PVP^- \rightarrow [EY]_{red} + PVP \quad \text{(v)}$$

$$[CdS]_{ox} + PVP^- \rightarrow [CdS]_{red} + PVP \quad \text{(vi)}$$

$$[EY]_{ox} + H_2SO_4 \rightarrow [EY]_{ox}\left[SO_4^{2-}\right] + 2H^+ \quad \text{(vii)}$$

$$[EY]_{ox}\left[SO_4^{2-}\right] + 2H^+ + e^- \rightarrow [EY]_{red} + H_2SO_4 \quad \text{(viii)}$$

$$[CdS]_{ox} + H_2SO_4 \rightarrow [CdS]_{ox}\left[SO_4^{2-}\right] + 2H^+ \quad \text{(ix)}$$

$$[CdS]_{ox}\left[SO_4^{2-}\right] + 2H^+ + e^- \rightarrow [CdS]_{red} + H_2SO_4 \quad \text{(x)}$$

During charging, the excitation of EY and CdS in the dye composite film results in the production of photoinduced electrons at the onset of light energy, and the simultaneous recombination of the same electrons during discharging of the device can be well explained by the abovementioned equations [51–54].

The electrons are drained incessantly through the PVP and $H_2SO_4$ portion, resulting in the overall charge separation at the boundaries of the acting electrodes and the high dielectric MP 0.09 thin film, which in turn enhances the potential difference and results in the concurrent increase in the photovoltage of our fabricated SPPB device. Upon reaching the maximum open circuit voltage of 1.17 V, the current in the circuit ceases. The device stability is quite commendable, as even after 30 days, the memorized voltage is considerably retained. Irreversible redox reactions resulting from electron loss in the external circuit may be responsible for the slight loss in photovoltage generation over time. No external bias is necessary for the successful operation of SPPB2.

The mechanism elucidated above is simple and analogous to that in our previous study [8]. We had earlier promised to work on the performance of these devices, and "SPPB2" is assuredly an improvement and a potential new approach for energy fields. Further development of the photovoltaic efficiency of photogenerated energy storage devices by calculating the optimization of the active material, carefully selecting the photon absorber material, and packaging the integrated device are our subjects of concern in future studies. Nevertheless, SPPB2 is a simple and cost-effective archetype device with remarkably impressive values of energy density, power density, and storage ability that should rise to a prominent level in the self-powered photovoltaics, energy conversion, and storage sectors.

## Conclusion

To briefly summarize, synthesizing electroactive and high dielectric thin MP film composites with the incorporation of in situ-synthesized $MgO_2$ NPs in a PVDF matrix to reconnoiter its potential as a self-charging energy storage medium was the major objective of our study. The results of the current research are good. The $\alpha$ crystals, dominating the pure matrix of PVDF, successfully nucleate into $\beta$ crystallites owing to the effective and homogeneous incorporation of in situ-synthesized $MgO_2$ NPs, and this noteworthy phase transformation is caused by the formation of long TTTT chains throughout the polymer matrix. Of all the tested concentrations, the MP 0.03 film showed the highest $\beta$-phase formation, i.e., $F(\beta)$ ~87%. A substantial enhancement happened in the dielectric constant with the addition of the in situ dopants into the polymer matrix, and the value increased up to the order of $10^6$ for the highest loading MP 0.09 films at 20 Hz. As an optimization, we utilized our synthesized film MP 0.09 with both a high phase and dielectric constant in the fabrication of a simple yet reasonably low-cost energy storage device. A film consisting of EY and $CdS/TiO_2/PVP/H_2SO_4$ is used as a photon absorber material. Under illumination, the open circuit output voltage achieved is 1.17 V in just 24 s, and the voltage is retained by our device for many hours even after the source of light is removed. Remarkable energy density and areal capacitance values of 240 mW h/m$^2$ and 1264 F/m$^2$, respectively, an admirable recycling ability for 30 days and hands-on applicability for powering modern electronic devices, e.g., LEDs and digital watches, give our device high potential for use in the practical world. We are quite hopeful that in the near future large-scale integration of this device, if carried out, will surely help the contemporary energy scarcity to a notable extent.

**Acknowledgements** The authors would like to acknowledge and convey their heartfelt appreciation for the monetary aid provided by the University Grants Commission (UGC) Govt. of India that allowed this research work to be conducted.

## Compliance with ethical standards

**Conflict of interest** The authors declare that they have no conflict of interest.



## References

1. Martins P, Lopes AC, Lanceros-Mendez S. Electroactive phases of poly(vinylidene fluoride): determination, processing and applications. Prog Polym Sci. 2014;39:683–706.
2. Martins P, Nunes JS, Hungerford G, Miranda D, Ferreira A, Sencadas V, et al. Local variation of the dielectric properties of poly(vinylidene fluoride) during the [alpha]- to [beta]-phase transformation. Phys Lett A. 2009;373:177–80.
3. Martins P, Caparros C, Goncalves R, Martins PM, Benelmekki M, Botelho G, et al. Role of nanoparticle surface charge on the nucleation of the electroactive β-poly(vinylidene fluoride) nanocomposites for sensor and actuator applications. J Phys Chem C. 2012;116:15790–4.
4. Ribeiro C, Sencadas V, Gomez Ribelles JL, Lanceros-Méndez S. Influence of processing conditions on polymorphism and nanofiber morphology of electroactive poly(vinylidene fluoride) electrospun membranes. Soft Mater. 2010;8:274–87.
5. Sencadas V, Gregorio Filho R, Lanceros-Méndez S. Processing and characterization of a novel nonporous poly(vinilidene fluoride) films in the β phase. J Non-Cryst Solids. 2006;352:2226–9.
6. Lim SH, Rastogi AC, Desu SB. Electrical properties of metal-ferroelectric-insulator-semiconductor structures based on ferroelectric polyvinylidene fluoride copolymer film gate for non-volatile random-access memory application. J Appl Phys. 2004;96:5673–82.
7. Hoque NA, Thakur P, Roy S, Kool A, Bagchi B, Biswas P, et al. $Er^{3+}/Fe^{3+}$ stimulated electroactive, visible light emitting, and high dielectric flexible PVDF film based piezoelectric nanogenerators: a simple and superior self-powered energy harvester with remarkable power density. ACS Appl Mater Interfaces. 2017;9:23048–59.
8. Roy S, Thakur P, Hoque NA, Bagchi B, Sepay N, Khatun F, et al. Electroactive and high dielectric folic acid/PVDF composite film rooted simplistic organic photovoltaic self-charging energy storage cell with superior energy density and storage capability. ACS Appl Mater Interfaces. 2017;9:24198–209.

9. Li Q, Wang Q. Ferroelectric polymers and their energy-related applications. Macromol Chem Phys. 2016;217:1228–44.
10. Kim GH, Hong SM, Seo Y. Piezoelectric properties of poly (vinylidene fluoride) and carbon nanotube blends: β-phase development. Phys Chem Chem Phys. 2009;11:10506–12.
11. Andrew JS, Clarke DR. Effect of electrospinning on the ferroelectric phase content of polyvinylidene difluoride fibers. Langmuir. 2008;24:670–2.
12. Das-Gupta DK, Doughty K. Corona charging and the piezoelectric effect in polyvinylidene fluoride. J Appl Phys. 1978;49:4601–3.
13. Bao SP, Liang GD, Tjong SC. Effect of mechanical stretching on electrical conductivity and positive temperature coefficient characteristics of poly(vinylidene fluoride)/carbon nanofiber composites prepared by non-solvent precipitation. Carbon. 2011;49:1758–68.
14. Mandal D, Henkel K, Schmeißer D. The electroactive β-phase formation in poly(vinylidene fluoride) by gold nanoparticles doping. Mater Lett. 2012;73:123–125.
15. Xu HP, Dang ZM. Electrical property and microstructure analysis of poly(vinylidene fluoride)-based composites with different conducting fillers. Chem Phys Lett. 2007;438:196–202.
16. Thakur P, Kool A, Bagchi B, Das S, Nandy P. Effect of in situ synthesized $Fe_2O_3$ and $Co_3O_4$ nanoparticles on electroactive β phase crystallization and dielectric properties of poly(vinylidene fluoride) thin films. Phys Chem Chem Phys. 2015;17:1368–78.
17. Wu W, Huang X, Li S, Jiang P, Toshikatsu T. Novel three-dimensional zinc oxide superstructures for high dielectric constant polymer composites capable of withstanding high electric field. J Phys Chem C. 2012;116:24887–95.
18. Deepa KS, Gopika MS, James J. Influence of matrix conductivity and coulomb blockade effect on the percolation threshold of insulator–conductor composites. Compos Sci Technol. 2013;78:18–23.
19. Priya L, Jog JP. Polymorphism in intercalated poly(vinylidene fluoride)/clay nanocomposites. J Appl Polym Sci. 2003;89: 2036–40.
20. Thakur P, Kool A, Bagchi B, Das S, Nandy P. Enhancement of β phase crystallization and dielectric behavior of kaolinite/halloysite modified poly(vinylidenefluoride) thin films. Appl Clay Sci. 2014;99:149–59.
21. Roy S, Thakur P, Hoque NA, Bagchi B, Das S. Enhanced electroactive β-phase nucleation and dielectric properties of PVdF-HFP thin films influenced by montmorillonite and Ni $(OH)_2$ nanoparticle modified montmorillonite. RSC Adv. 2016; 6:21881–94.
22. Yuan J-K, Yao S-H, Dang Z-M, Sylvestre A, Genestoux M, Bai J. Giant dielectric permittivity nanocomposites: realizing true potential of pristine carbon nanotubes in polyvinylidene fluoride matrix through an enhanced interfacial interaction. J Phys Chem C. 2011;115:5515–21.
23. Zhou T, Zha JW, Cui RY, Fan BH, Yuan JK, Dang ZM. Improving dielectric properties of BaTiO3/ferroelectric polymer composites by employing surface hydroxylated BaTiO3 nanoparticles. ACS Appl Mater Interfaces. 2011;3:2184–8.
24. Martins P, Costa CM, Benelmekki M, Botelho G, Lanceros-Mendez S. On the origin of the electroactive poly(vinylidene fluoride) β-phase nucleation by ferrite nanoparticles via surface electrostatic interaction. CrystEngComm 2012;14:2807–11.
25. Eswaraiah V, Sankaranarayanan V, Ramaprabhu S. Functionalized graphene-PVDF foam composites for emi shielding. Macromol Mater Eng. 2011;296:894–8.
26. Thakur P, Kool A, Bagchi B, Hoque NA, Das S, Nandy P. In situ synthesis of $Ni(OH)_2$ nanobelts modified electroactive poly (vinylidene fluoride) thin films: remarkable improvement in dielectric properties. Phys Chem Chem Phys. 2015;17:13082–91.
27. Chu S, Majumdir A. Opportunities and challenges for a sustainable energy future. Nature 2012;488:294–303.
28. Wang H, Dai H. Strongly coupled inorganic–nano-carbon hybrid materials for energy Storage. Chem Soc Rev. 2013;42:3088–113.
29. Rosa EA, Dietz T. Human drivers of national greenhouse-gas emissions. Nat Clim Change. 2012;2:581–6.
30. Khatun F, Hoque NA, Thakur P, Sepay N, Roy S, Bagchi B, et al. 4′-chlorochalcone-assisted electroactive polyvinylidene fluoride film-based energy-storage system capable of self-charging under light. Energy Technol. 2017;5:1–12.
31. Lo C-W, Li C, Jiang H. Direct solar energy conversion and storage through coupling between photoelectrochemical and ferroelectric effects. AIP Adv. 2011;1:042104.
32. Xin X, He M, Han W, Jung J, Lin Z. Low-cost copper zinc tin sulfide counter electrodes for high efficiency dye-sensitized solar cells. Angew Chem. 2011;50:11739–42.
33. Wu J, Lan Z, Hao S, Li P, Lin J, Huang M, et al. Progress on the electrolytes for dye-sensitized solar cells. Pure Appl Chem. 2008;80:2241–58.
34. Cha SI, Kim Y, Hwang KH, Shin Y-J, Seo SH, Lee DY. Dye-sensitized solar cells on glass paper: Tco-free highly bendable dye-sensitized solar cells inspired by the traditional korean door structure. Energy Environ Sci. 2012;5:6071.
35. Chen T, Qiu L, Yang Z, Cai Z, Ren J, Li H, et al. An integrated "energy wire" for both photoelectric conversion and energy storage. Angew Chem. 2012;5:11977–80.
36. Chien CT, Hiralal P, Wang DY, Huang I, Chen CC, Chen CW, et al. Graphene-based integrated photovoltaic energy harvesting/storage device. Small. 2015;11:2929–37.
37. Zhang M, Zhou QQ, Chen J, Yu XW, Huang L, Li YR, et al. An ultrahigh-rate electrochemical capacitor based on solution-processed highly conductive PEDOT: PSS films for ac line-filtering. Energy Environ Sci. 2016;9:2005–10.
38. Xu J, Chen Y, Dai L. Efficiently photo-charging lithium-ion battery by perovskite solar cell. Nat Commun. 2015;6:1–7.
39. Murakami TN, Kawashima N, Miyasaka TA. High-voltage dye-sensitized photocapacitor of a three-electrode system. Chem Commun. 2005;26:3346–8.
40. Zhou F, Ren Z, Zhao Y, Shen X, Wang A, Li YY, et al. Perovskite photovoltachromic supercapacitor with all-transparent electrodes. ACS Nano. 2016;10:5900–8.
41. Thakur P, Kool A, Hoque NA, Bagchi B, Khatun F, Biswas P, et al. Superior performances of in situ synthesized ZNO/PVDF thin film based self-poled piezoelectric nanogenerator and self-charged photo-power bank with high durability. Nano Energy. 2018;44:456–67.
42. Wee G, Salim T, Lam YM, Mhaisalkar SG, Srinivasan M. Printable photo-supercapacitor using single-walled carbon nanotubes. Energy Environ Sci. 2011;4:413–6.
43. Dakin TW. Conduction and polarization mechanisms and trends in dielectrics. IEEE Electr Insul Mag. 2006;22:11–28.
44. Li Y, Huang X, Hu Z, Jiang P, Li S, Tanaka T. Large dielectric constant and high thermal conductivity in poly(vinylidene fluoride)/barium titanate/silicon carbide three-phase nanocomposites. ACS Appl Mater Interfaces. 2011;3:4396–403.
45. Lopes AC, Costa CM, Sabater i Serra R, Neves IC, Gomez Ribelles JL, Lanceros-Méndez S. Dielectric relaxation, ac conductivity and electric modulus in poly(vinylidenefluoride)/nay zeolite composites. Solid State Ion. 2013;235:42–50.
46. Wang J-W, Wang Y, Wang F, Li S-Q, Xiao J, Shen Q-D. A large enhancement in dielectric properties of poly(vinylidene fluoride) based all-organic nanocomposite. Polymer. 2009;50:679–84.
47. Yin Y, Feng K, Liu C, Fan SA. Polymer supercapacitor capable of self-charging under light illumination. J Phys Chem C. 2015;119:8488–849.

48. Shi C, Dong H, Zhu R, Li H, Sun Y, Xu D, et al. An "all-in-one" mesh-typed integrated energy unit for both photoelectric conversion and energy storage in uniform electrochemical system. Nano Energy. 2015;13:670–8.
49. Hou K, Tian B, Li F, Bian Z, Zhao D, Huang C. Highly crystallized mesoporous $TiO_2$ films and their applications in dye sensitized solar cells. J Mater Chem. 2005;15:2414–20.
50. Mohapatra SK, Kondamudi N, Banerjee S, Misra M. Functionalization of self-organized $TiO_2$ nanotubes with Pd nanoparticles for photocatalytic decomposition of dyes under solar light illumination. Langmuir. 2008;24:11276–81.
51. Zhang X, Huang X, Li C, Jiang H. Dye-sensitized solar cell with energy storage function through PVDF/ZNO nanocomposite counter electrode. Adv Mater. 2013;25:4093–6.
52. Biswas P, Hoque NA, Thakur P, Saikh MdM, Roy S, Khatun F, et al. Highly efficient and durable piezoelectric nanogenerator and photo-power cell based on CTAB modified montmorillonite incorporated PVDF film. ACS Sustain Chem Eng. 2019; 7:4801–13.
53. Khatun F, Thakur P, Kool A, Roy S, Hoque NA, Biswas P, et al. Photo-rechargeable organic–inorganic dye-integrated polymeric power cell with superior performance and durability. Langmuir. https://doi.org/10.1021/acs.langmuir.9b00622.
54. Skunik-Nuckowska M, Grzejszczyk K, Kulesza PJ, Yang L, Vlachopoulos N, Häggman L, et al. Integration of solid-state dye-sensitized solar cell with metal oxide charge storage material into photoelectrochemical capacitor. J Power Sources. 2013;23:491–99.